RSC Advances

PAPER

View Article Online
View Journal | View Issue

Cite this: *RSC Adv.*, 2024, **14**, 27789

Close-packed nitronyl nitroxide radicals by Au–S self-assembly: strong ferromagnetic coupling†

Zhipeng Xu,[a] Yongliang Qin,[b] Dongdong Wei,[a] Jie Jin,[a] Long Zheng,[a] Jie Xu,[a] Hui Liu,[a] Ranran Chen[a] and Di Wang *[a]

Received 20th June 2024
Accepted 26th August 2024

DOI: 10.1039/d4ra04506h

rsc.li/rsc-advances

The study of the magnetism of tightly arranged nitronyl nitroxide (**NN**) radicals *via* Au–S self-assembly is interesting. In this study, a series of radicals (**S-NN**, **D-NN**, **BS-NN**, **BD-NN**) along with two types of nanomaterials (**S-NPs**, **D-NPs**) were synthesized. **NN** was chosen for the magnetic units. Their structures have been successfully synthesized and analyzed. The spin magnetic properties were characterized by electron paramagnetic resonance (EPR) and superconducting quantum interference device (SQUID) measurement. The analysis revealed that the self-assembled **NN** formed *via* Au–S bonds exhibits high packing density. Furthermore, it was gratifying to observe that the AuNPs exhibit ferromagnetism after the surface modification by **NN**. This results in strong ferromagnetic exchange interactions of **S-NPs** and **D-NPs** : $J_{\text{S-NPs}} = +279.715$ K and $J_{\text{D-NPs}} = +254.913$ K, respectively.

Introduction

In recent years, organic magnetic hybrid materials have attracted a lot of interest from scientists. These materials combine the predictable low density, ease of processing,[1,2] structural tunability and diversity of organic materials with the magnetic functionality found in magnetic materials. An important task in the design of these organic magnetic hybrid materials is the integration of organic structure with magnetic properties. Many studies have focused on organic–inorganic hybrid magnets, which integrate inorganic components with organic molecules within a unified structure, have been synthesized to control the magnetic properties of materials.[3–5] However, the magnetic properties of such materials rely on the inorganic components, thereby somewhat limiting the combination of organic structure with magnetic properties. Organic intrinsic magnets[6] are a class of organic magnetic materials in which the aggregation of unpaired electrons[7] within organic structures leads to the emergence of magnetic properties.[8] Current research on organic intrinsic magnets predominantly focuses on the field of molecules. Different stable radicals, such as TEMPO,[9] **NN**,[10–12] PTM,[13] *etc.*, were used in the research. For single radicals, their crystal arrangement, and magnetic characteristics have been extensively characterized and investigated by introducing hydrogen bonds, ligand groups or diverse bridging structures. Some progress has been made in studying the structural properties and functionalization of organic intrinsic magnets. However, compared to traditional iron–cobalt–nickel series magnets,[14,15] the aggregated state magnetism of organic intrinsic magnets is relatively weak. Therefore, it is desirable to employ the self-assembly strategy to design organic magnetic hybrid materials with good aggregated state magnetism.

NN, a stable neutral organic radical with good spin delocalization properties and large value of spin polarization at room temperature[16–21] has been extensively studied for its excellent spin magnetic properties and serves as a promising candidate for magnetic units. Self-assembly[13,22–25] is a technique wherein fundamental units spontaneously organize into an ordered and dense structure. Gold nanoparticles[26–28] possess advantages of adjustable shape and size, large specific surface area, facile synthesis, surface modification capabilities, and excellent biocompatibility, which have attracted more and more attention. The technology of functionalization on the surface of gold nanoparticles by Au–S self-assembly has been quite mature.

V. Loveras *et al.* proposed a one-pot reaction method for obtaining monodisperse[22] gold nanoparticles, which can be utilized to synthesize organic radical-functionalized gold nanoparticles with controllable size, uniform morphology, and stable properties. However, this study did not conduct qualitative and quantitative analysis of the aggregated magnetic properties of the synthesised magnetic materials.

Herein, we present the synthesis and characterization of several novel self-assembled agglomerated organic materials. **NN** was selected as the magnetic unit, and the Au–S self-assembly strategy was employed to enhance the close packing of organic spin units. The synthesis of **NN** section is based on the previously reported reference, combined with the general

[a]*School of Materials Science and Chemical Engineering, Anhui Jianzhu University, Hefei 230601, China. E-mail: wangdi@ahjzu.edu.cn*

[b]*Anhui Province Key Laboratory of Condensed Matter Physics at Extreme Conditions, Hefei Institutes of Physical Science, Chinese Academy of Sciences, Hefei, Anhui 230031, China*

† Electronic supplementary information (ESI) available. See DOI: https://doi.org/10.1039/d4ra04506h

synthesis steps[18] developed by our group. Long flexible organic chains were chosen for self-assembly on the gold surface to facilitate vertical alignment and dense packing.[24,29] The specific synthesis pathway is shown in Fig. 1a. Subsequently, monodisperse gold nanoparticles (**AuNPs**) with uniform particle size were selected and synthesized according to reported procedures. At room temperature, the synthesized bi-single nitronyl nitroxide (**BS-NN**) and bi-double nitronyl nitroxide (**BD-NN**) are added to the nanoparticles. Based on the Au–S interaction, the disulfide bonds were broken, and self-assembled on the surface of the **AuNPs**. Single radical self-assembled gold nanoparticles (**S-NPs**) and double radical self-assembled gold nanoparticles (**D-NPs**) were obtained, respectively. The synthesis diagram is shown in Fig. 1b. The products were characterized and analyzed through UV-vis, IR, CV, TEM, SEM, EDS, DLS measurements. Furthermore, RT-EPR, VT-EPR and SQUID measurements

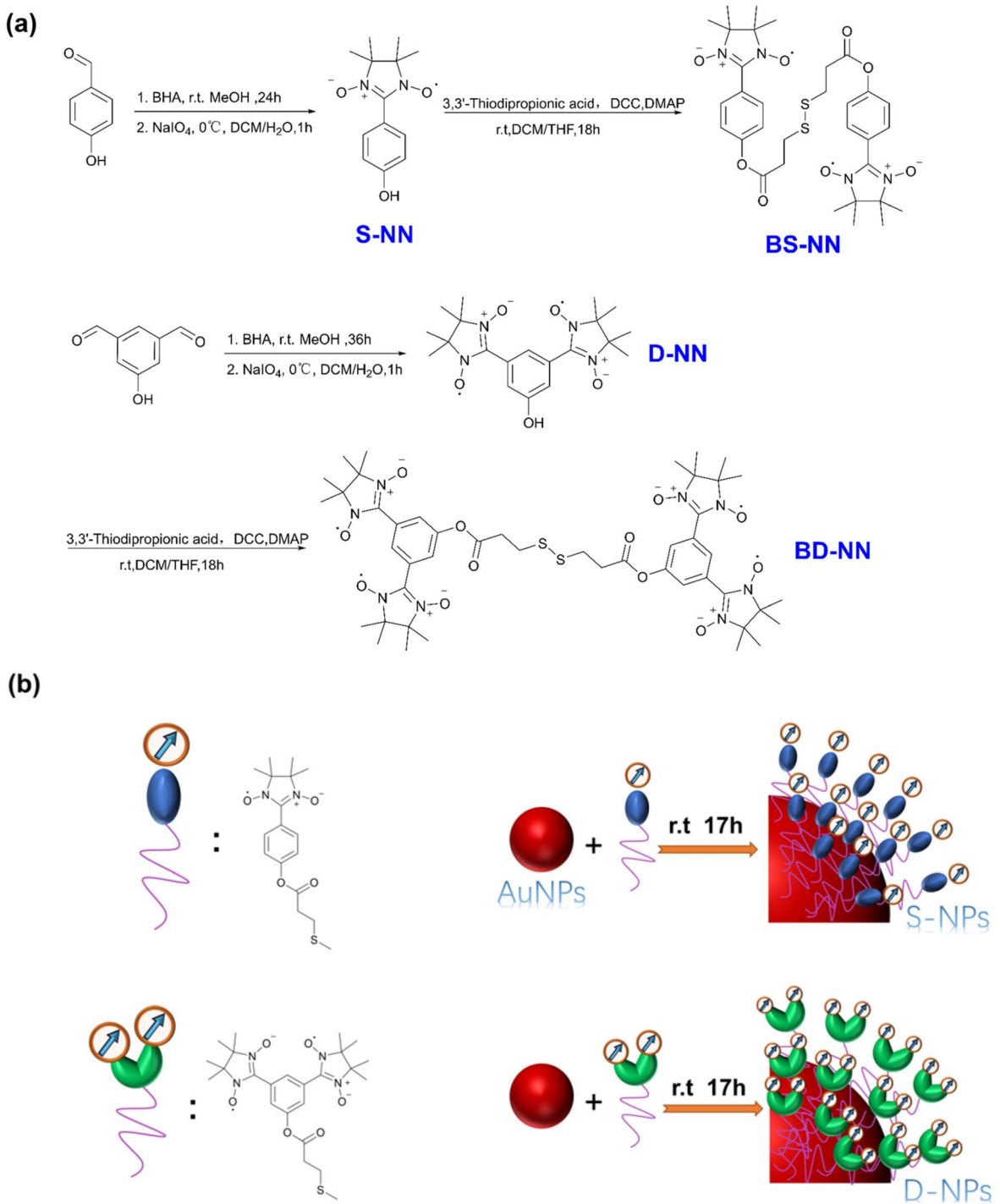

Fig. 1 (a) Synthesis flow chart of S-NN, BS-NN, D-NN and BD-NN; (b) composite concept diagram of S-NPs and D-NPs. The red ball refers to trioctylamine stabilized gold nanoparticles.

revealed the strong ferromagnetic interactions in both **S-NPs** and **D-NPs**, and DFT calculations were performed to collect information about the electronic structure of them (Fig. S9†).

Experimental

Materials

All products used were purchased from aladdin and have not been further purified unless otherwise specified. The compound 2,3-bis(hydroxy-amino)-2,3-dimethylbutane (BHA)[19] was synthesized as described in the literature. All reaction units were dried in a blast dryer and synthesized in a dry argon atmosphere.

General considerations

Unless otherwise noted, CW X-band EPR spectra are recorded in toluene diluted and oxygen-free solutions at concentrations of 10^{-4} moles. G-factor correction using 2,2-diphenyl-1-picrohydrazine ($g = 2.00370$) as standard, equipped with a frequency counter and liquid helium flow temperature control, simulated with WINEPR SimFonia software. All electrochemical measurements were performed using CHI760E (Shanghai Chenhua, China). Elemental analysis was performed by scanning electron microscopy (SEM JSM-7500F) and mapping. The phase structure of the samples was ascertained by X-ray diffraction (XRD, Bruker, D8-ADVANCE) and Raman spectra (Renishaw InVia Raman spectrometer). The organic structure was verified using the liquid-mass spectrometer (Waters xevo TQD). Transmission electron microscope (Hitachi HITACHI-HT7700) was used to observe the morphology of the sample, and the average particle size of the sample was calculated by imageJ. The particle size of the sample was analyzed using a particle size analyzer (Malvern Instr, UK). Fourier transform infrared spectroscopy (Nicolet6700) was used to determine the functional groups of the samples. The UV-vis absorption spectra were recorded with Shanghai Jingke L7 spectrophotometer at room temperature. The spectroscopic experiments were carried out in toluene as solvent at room temperature. VT and VM susceptibility were measured using the Quantum Design MPS-XL-7 SQUID magnetization meter. The sample was wrapped with about 10 mg of Teflon tape and measured in a measuring tube, minus the background signal and diamagnetic correction of the gold nanoparticle sample.

Results and discussion

Optical properties

UV. We performed UV-vis measurements on materials. The characteristic UV peaks of **NN** appeared at 600 nm (Fig. 2a). The characteristic UV peaks of **AuNPs** appeared at 525 nm (Fig. 2b). Both the prepared **S-NPs** and **D-NPs** exhibited distinct absorption peaks corresponding **AuNPs**, with the intensity of **NN** characteristic peaks of **D-NPs** was higher at the same molar concentration of **AuNPs**, which suggests that a larger density of **NN** packing was achieved by **D-NPs**. By comparing the characteristic peaks of **NPs** and **NN** at the same molar concentration of

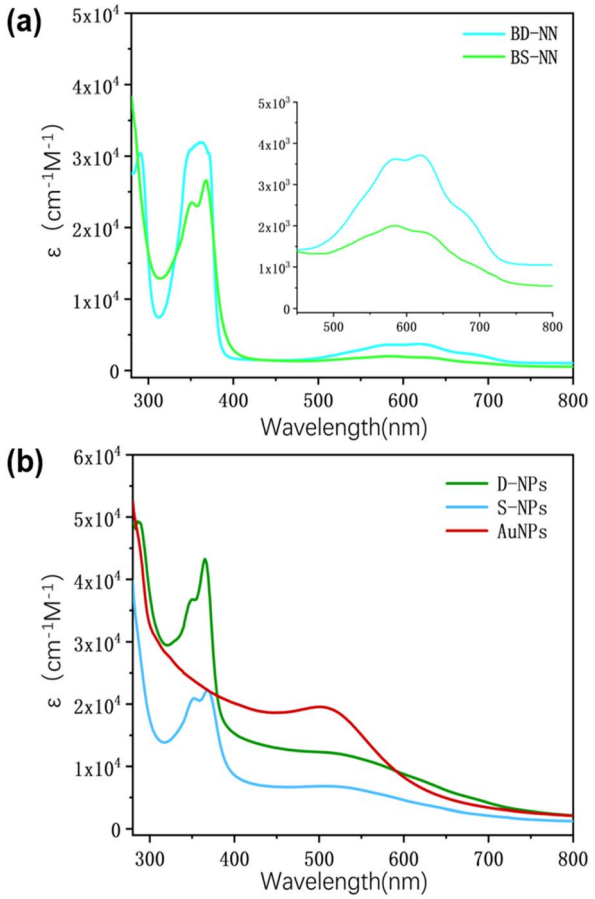

Fig. 2 (a) UV spectra of **BS-NN** and **BD-NN**; (b) UV spectra of AuNPs, **S-NPs** and **D-NPs**. Tests were performed at the same concentration.

AuNPs, the proportion of B-radicals grafted onto **AuNPs** in relation to the radicals introduced into the reaction can be calculated semi-quantitatively. According to the analysis of **S-NPs** and **D-NPs** signal strength with equal concentration of gold nanoparticle signal deducted, the graft proportion of **BS-NN** is determined to be 19%, while that of **BD-NN** is 31%.

IR. Infrared spectroscopy (IR) testing enables the characterization of functional groups present in materials. Therefore, we conducted IR spectroscopy analysis on all samples. Fig. 3a illustrates that **S-NN** and **D-NN** exhibited a broad and strong stretching vibrational peak of hydroxyl group at 3300 cm^{-1}. **BS-NN** and **BD-NN** showed a stretching vibrational peak of C=O at 1720 cm^{-1}, and a stretching vibrational peak of C–O–C at 1200 cm^{-1}. The appearance of the characteristic vibrational peak of S–S, indicating the successful synthesis of the ester bond. As shown in Fig. 3b, the characteristic peaks of ester bond were retained near 1720 cm^{-1} and 1200 cm^{-1} for **S-NPs** and **D-NPs**. Additionally, the characteristic peaks of S–S disappeared between 500–600 cm^{-1}, signifying the successful synthesis of **NPs** based on gold–sulfur self-assembly, where the disulfide bond had been broken and self-assembly with gold had occurred.

Raman spectrum and XRD. In order to further verify the successful conduct of self-assembly, Raman spectroscopy and XRD tests were performed on substances (**BS-NN**, **BD-NN**, **S-NPs**

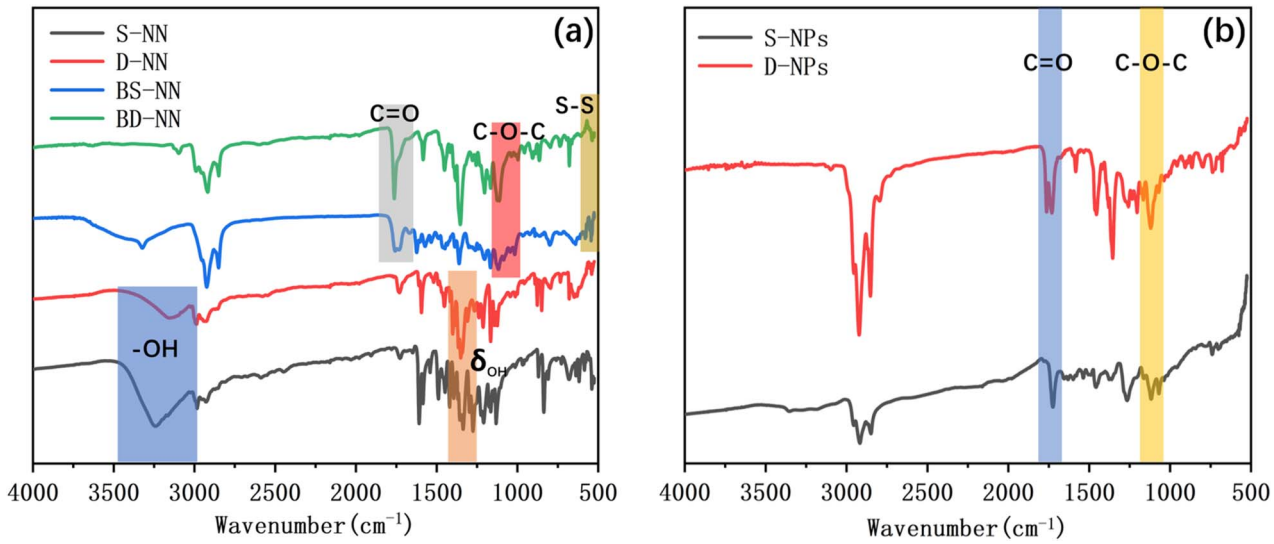

Fig. 3 (a) IR spectrum of S-NN, D-NN, BS-NN and BD-NN; (b) IR spectrum of S-NPs and D-NPs.

and **D-NPs**) before and after self-assembly (Fig. 4). We found that NPs after self-assembly peaks near 280 cm^{-1}, indicating that Au–S bonds are formed during self-assembly.[30] We conducted XRD tests on polystyrene fixed samples. However, no obvious peaks ascribed to Au can be observed *via* XRD, indicating that the nanoparticles we prepared are very small and well dispersed.[31,32] This is in accordance with the TEM and ζ particle size characterizations.

Electrochemical studies. Cyclic voltammetry (CV) was employed to qualitatively detect nitronyl nitroxide. Fig. 5 summarizes the resulting test data. The appropriate test voltage range was selected, and the wider voltage test data can be found in Fig. S1.† The spectrum of **BS-NN** have been previously reported.[22] The spectrum of **BD-NN** exhibited a reversible redox wave with $E_{1/2} = 370$ mV (Fig. 5a). At a scanning rate of 100 mV s^{-1}, the oxidation potential occurred at 456 mV and the reduction potential appeared at 292 mV, respectively, with a difference of $\Delta E = 164$ mV. This electrochemical quasi-reversible process arises from the nitroxide–nitroxide radical molecule. Cyclic voltammetry of **S-NPs** exhibited a reversible redox wave with $E_{1/2} = 430$ mV (Fig. 5b). The oxidation potential occurred at 494 mV and the reduction potential appeared at 364 mV at the scan rate of 100 mV s^{-1}. The redox peak was attributed to nitronyl nitroxides on the surface of the **NPs**. A pair of weaker redox peaks near 820 mV may be attributed to the radical spatial interactions resulting from the tight aggregation of radicals on the surface of **AuNPs**. The oxidation potential of **D-NPs** were 479 mV and 815 mV, while the reduction potential were 364 mV and 733 mV (Fig. 5c). The voltage difference between the anodic peaks and the cathodic peaks ($\Delta E = 99$ mV) was 64 mV smaller than that of **BD-NN** in solution ($\Delta E = 163$ mV), which is due to the adsorption of electroactive molecules on the surface of **AuNPs**. This phenomenon indicates a fast diffusion process. This splitting of the redox peak can be explained by the interaction between the radical components. The first redox peak exhibited higher intensity compared to the second redox peak, which may be attributed to a small error in the testing performed with ferrocene as a reference electrode. It has been reported that a second redox peak occurs with higher radical packing density, and two pairs of redox peaks were observed for **S-NPs** and **D-NPs**, with the second redox peak being more prominent for **D-NPs**, supporting the achievement of a greater radical packing density achieved by **D-NPs**.

In addition, an increase in the scanning rate led to higher peak intensities, as observed from the CV data. This result can be attributed to surface-restricted electroactive substances, further confirming the successful preparation of radical-grafted nanoparticles. Furthermore, multiple groups of tests under the same conditions yielded nearly identical redox waves and current intensities, enhancing the accuracy of this dataset.

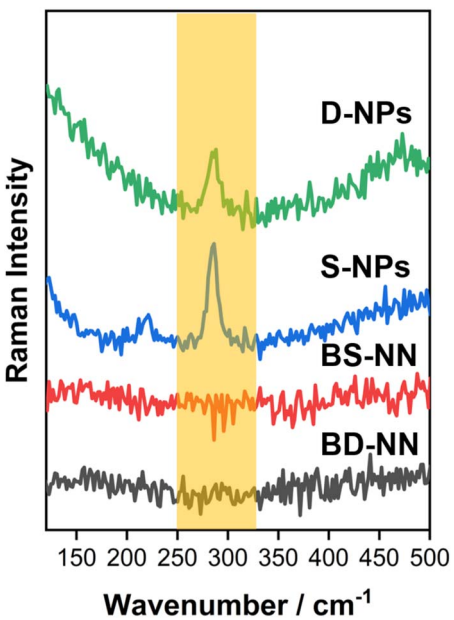

Fig. 4 Raman spectrum of BS-NN, BD-NN, S-NPs and D-NPs.

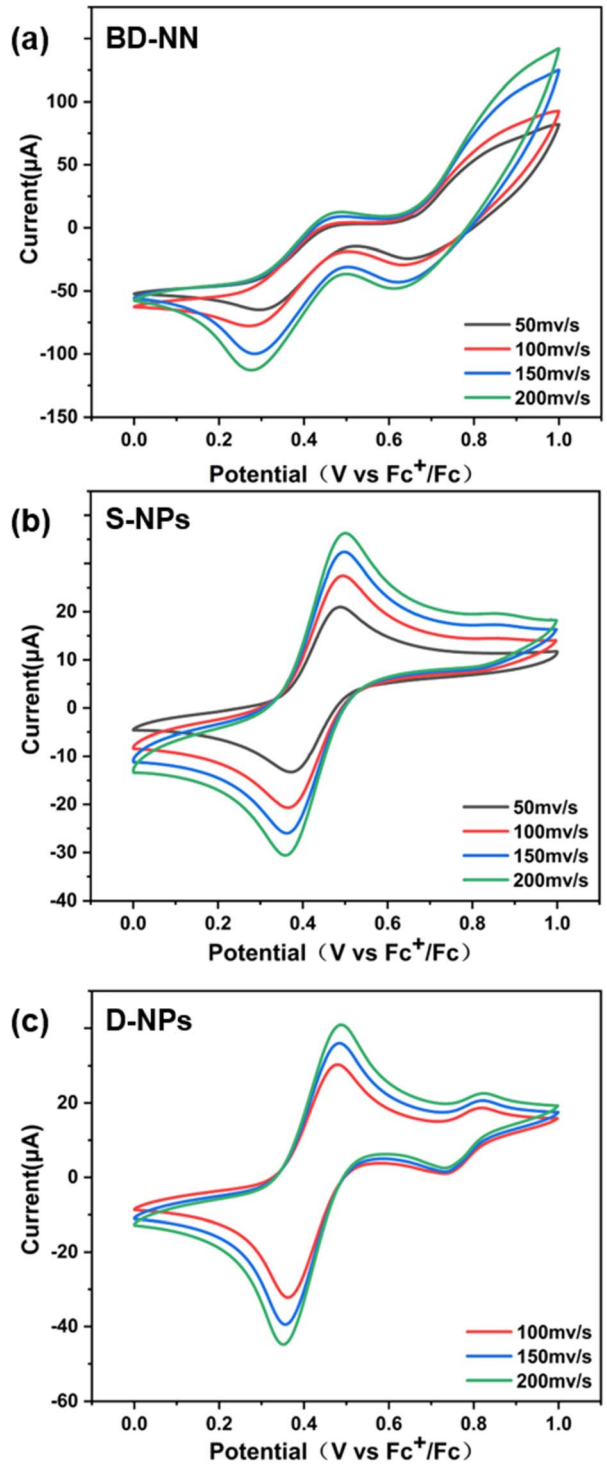

Fig. 5 (a) CV spectrum of **BD-NN**; (b) CV spectrum of **S-NPs**; (c) CV spectrum of **D-NPs**. Each set of tests adopts 50 mV s^{-1}, 100 mV s^{-1}, 150 mV s^{-1}, and 200 mV s^{-1} sweep speeds. The CVs were all tested in CH_3CN with 0.02 M tetrabutylammonium hexafluorophosphate as electrolyte and Pt as working electrode.

Discussion of radicals packing density

TEM. We conducted transmission electron microscopy (TEM) analysis to examine the samples. The test results (Fig. 6a and c)

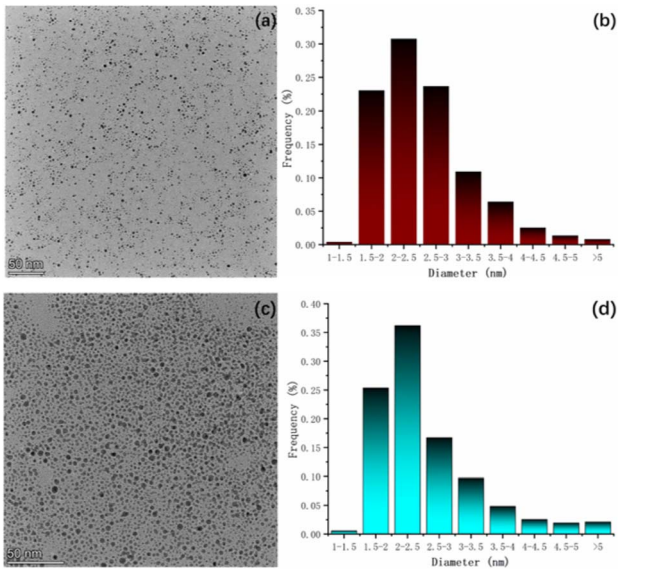

Fig. 6 (a) TEM spectrum of **S-NPs**; (b) statistical graph of particle size of **S-NPs**; (c) TEM spectrum of **D-NPs**; (d) statistical graph of particle size of **D-NPs**.

revealed that the **S-NPs** exhibited excellent dispersion, and nearly all of them appeared spherical in shape. The sample data were statistically analyzed using ImageJ software (Fig. 6b and d), which calculated the average particle size of **S-NPs** was 2.57 nm, primarily distributed within the range of 1.5–3 nm. Similarly, the average particle size of **D-NPs** was determined to be 2.54 nm, mainly distributed within the range of 1.5–2.5 nm. Particle size was also validated by DLS data (Fig. S6†).

The slightly smaller particle size of **D-NPs** compared to **S-NPs** can be attributed to the structural characteristics of the radicals involved. Firstly, the linear structure of the double radicals is not as long as that of the single radicals. Secondly, the linear structure of the double radicals is not as bulky as that of the single radicals. These factors contribute to the smaller size of **D-NPs**. The stereo-hindrance effect leads to an increase in the packing density of the **NN** moiety but a decrease in the packing density of the flexible chain moiety. Consequently, the organic portion's content is reduced, resulting in smaller particle size for **D-NPs**.

EDS. In order to determine the elemental distribution of the samples, EDS tests were carried out on several synthesized

Table 1 SEM mapping test data of **AuNPs** and **S-NPs**, **D-NPs**

Product	Element	Line type	Weight%	Atomic%
AuNPs	Au	M series	97.38	72.58
	N	K series	2.62	27.42
S-NPs	Au	M series	81.77	27.70
	S	K series	3.67	7.65
	N	K series	6.59	31.41
	O	K series	7.97	33.24
D-NPs	Au	M series	55.91	10.39
	S	K series	13.08	14.94
	N	K series	11.42	29.85
	O	K series	19.58	44.82

Table 2 Relevant data calculated based on SEM and EDS/mapping test data

Product	Particle diameter (nm)	AuNPs area (Å^2)	The average number of **NN** per AuNP	Maximum packing density S_0 (Å^2)
S-NPs	2.57	2075	157	13.2
D-NPs	2.54	2027	728	2.8

samples, respectively (Fig. S2–S5†). The test spectra are presented in Fig. S2–S5.† The data were averaged over the four groups tested and statistically presented in Table 1, and the counting calculation data are shown in Table 2. The calculation reveal that the self-assembled density of **S-NPs** is 13.2 Å^2, which is different from the previous reports. This discrepancy can be attributed to the following three reasons: (i) different elements selected for counting radicals; (ii) variances in the radii of prepared nanoparticles; (iii) variations in specific surface area. The self-assembled density of **D-NPs** is 2.8 Å^2, indicating a significant increase in the packing density compared to **S-NPs**.

Both **S-NPs** and **D-NPs** were synthesized from the same batch of **AuNPs**, the influence of the **AuNPs** size can be excluded. The radical packing density of **D-NPs** is approximately 4.75 times higher than that of **S-NPs**, which can be attributed to three factors: (i) the **BD-NN** structure contains twice as many **NN** as **BS-NN**; (ii) interactions between the two radical groups in the *m*-phenylene diradical on the **D-NPs** may reduce the steric hindrance between the radical groups, thus contributing to a more ordered arrangement of the radicals on the **AuNPs**; (iii) the strong magnetic interactions between the radicals on the gold surface may facilitate their close packing. In summary, it can be concluded that self-assembly using multi-radicals is indeed an effective strategy for enhancing the compact packing of radicals.

Magnetic properties study

EPR. The EPR spectra of all radical-containing samples were tested at room temperature and fitted (Fig. 7) to obtain the relevant parameters (Table 3). Different gold-radical ratios were selected for the self-assembly of the samples (Fig. S7†), and the products were tested by EPR.

The packing molar ratio ($HAuCl_4$: **B-NN** = 5 : 1) was selected,[22] and the gradient test plots are shown in Fig. S7 and S8.† According to the previous reports,[33] at room temperature, the single radical of **NN** are five-line spectra, whereas the well-coupled double radicals present nine-line spectra. Fig. 7a illustrates **S-NN**, which shows a standard five-line spectra. The fitting results yields a g value of 2.00650 and a_N = 7.5 G, consistent with previous reports, which is consistent with typical **NN**-type single radical hyperfine splitting features.

Due to the flexible nature of the bi-radical skeleton in **BS-NN**, the coupling between the bi-radicals is primarily spatial, and the coupling strength is weak. As a result, the spectra differ

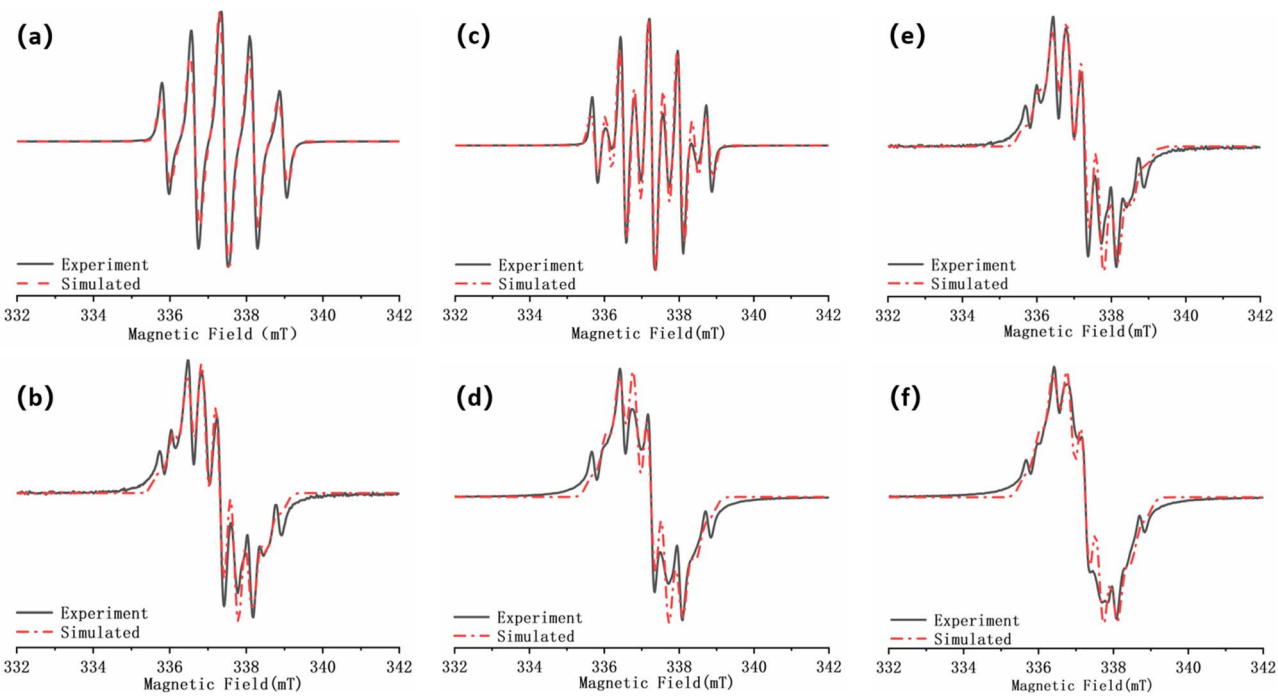

Fig. 7 (a) EPR spectrum of **S-NN**; (b) EPR spectrum of **D-NN**; (c) EPR spectrum of **BS-NN**; (d) EPR spectrum of **BD-NN**; (e) EPR spectrum of **S-NPs**; (f) EPR spectrum of **D-NPs**. The black curves are experimental data and the red curves are fitted data. (a), (b), (c), (d) were obtained by testing in DCM and (e), (f) were obtained by testing in toluene. All spectra were obtained at room temperature.

Table 3 EPR fits were performed to obtain g and $a_{N/2}$ values for all samples containing radicals

Sample	λ (nm)	ε (cm^{-1} M^{-1})	g	$a_{N/2}$ (G)	$\lvert D/hc\rvert$ (cm^{-1})	r (Å)
S-NN	—	—	2.00650	7.50	—	—
D-NN	—	—	2.00675	3.55	—	—
BS-NN	578 619	3 6853 744	2.00685	7.50	—	—
BD-NN	581 634	20 061 822	2.00690	3.65	0.00541	7.88
S-NPs	623	—	2.00690	3.70	0.00531	7.93
D-NPs	628	—	2.00690	3.55	0.00550	7.84

from the standard nine-line spectra of strongly interacting two-radicals, as verified in Fig. 7c. For **D-NN**, the fit yields the g value of 2.00675 and $a_N = 3.55$ G, which is about half of the hyperfine splitting in a typical **NN** single radical. However, the overall spectral line splitting is poorer (Fig. 7b). This can be attributed to the close proximity of the interstitial double radical on benzene, leading to strong intramolecular spin–spin interactions. When esterification is performed to synthesize **BD-NN** (Fig. 7d), the radicals within the molecule strongly interact with each other. Consequently, the uniformity of line splitting is further compromised. The EPR spectra of both **S-NPs** (Fig. 7e) and **D-NPs** (Fig. 7f) resemble the spectra of their precursor B-radicals when the **AuNPs** with maximum packing density are prepared at the suitable ratio. However, their linewidths closely approach their a_N value, resulting in poorer linewidth uniformity and signal intensity. This can be attributed to the close packing of radicals on the surface of **AuNPs**, which further strengthens the spatial coupling between the radicals.

When radicals are spatially close to the gold surface, spin conduction and coupling at the gold surface is achieved through complex spin–spin interactions (including spatial, chemical bonding, and spin off-domains on gold surface).[22] These interactions may contribute to the deterioration of the ultrafine cleavage fraction of EPR signals in the gold-nanoscale self-assembled samples.

In order to further investigate the magnetic coupling mechanism between the densely packed radicals on **AuNPs**, the cryogenic solution EPR spectra of all the samples in 10–100 K DCM were recorded, and the J values were obtained from the fitting of IT-T diagrams:[18] Fitting the plot of IT *versus* T gives $\Delta E_{S\text{-}T} = +130.69$ cal mol^{-1}, $2J\,k_B^{-1} = +66.89$ K for **S-NPs** and $\Delta E_{S\text{-}T} = +81.16$ cal mol^{-1}, $2J\,k_B^{-1} = +41.54$ K for **D-NPs** (Fig. 8) (Table 4). Among them, **BD-NN** and **D-NPs** exhibit clear $|\Delta M_s| = 2$ signals in the half-field (Fig. S8†). From the test spectra, the experimental parameter D value can be obtained. In general, a larger D value implies a closer intramolecular spin–spin distance. Using the point approximation, $2D = 3g^2\,\mu_B/r^3$, the dipole–dipole distance can be derived approximately and used to analyze the distances of neighboring spins within the molecule. The value of D depends on the dipole–dipole interactions in the spin–spin system and not directly on the exchange interactions. Consequently, the value of D reflects the spatial distance. Theoretically, the radical portions on **S-NPs** should be isolated from each other without intramolecular interactions. However, the disulfide bond-breaking self-assembly is a dynamically reversible process, and under high-density

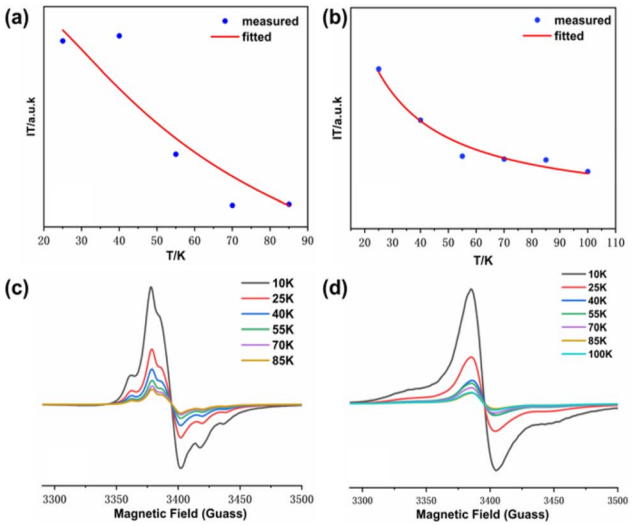

Fig. 8 (a) IT-T fitted images of **S-NPs**; (b) IT-T fitted images of **D-NPs**; (c) EPR spectra of **S-NPs** measured over a temperature gradient; (d) EPR spectra of **D-NPs** measured over a temperature gradient. All samples are solved in DCM for test.

packing conditions, it may partially convert back to **BS-NN**. On the other hand, it has been reported that the self-assembled radicals on the gold surface can result in a spin–spin interaction similar to the intramolecular spin–spin interactions. This explains the existence of certain intramolecular interactions in **S-NPs**. All tested and calculated data are shown in Fig. S8† and Table 3. The plot of IT *vs.* T was fitted with the transformed Bleaney–Bowers eqn (1).[34] Where **BS-NN** consistent with previously reported spectra,[22] exhibit a well-defined zero-field splitting (zfs) pattern, this is a typical EPR pattern for mono-radical phenyl nitronyl nitroxide. **BS-NN** shows a weak peak at $|\Delta M_s| = 2$, suggesting very weak dipole interactions within the molecule, mainly due to the excessive distances along the bond between the spin units. For **S-NPs**, $|D/hc| = 0.00531$ cm^{-1}, which calculates to an average spin–spin distance of 7.93 Å. For **D-NPs**, $|D/hc| = 0.00550$ cm^{-1}, which calculates to an average spin–spin distance of 7.84 Å. It can be clearly observed that **D-NPs** achieve smaller spin–spin distances relative to **S-NPs**. This implied that the **D-NPs** achieve higher radical packing densities.

The magnetic properties analyzed by the variable-temperature EPR test spectra are different from previously reported.[22] We believe that this difference is due to the lack of formula fitting and only empirical judgment in previous work. In fact, the thiol-modified gold nanoparticles are ferromagnetic,[35] and the radicals used for self-assembly are also ferromagnetic,[36] so the **NN** modified gold nanoparticles should also

Table 4 Magnetic properties of samples of **S-NPs** and **D-NPs**

Radicals	T_{conv}[a]/K	θ[b]/K	J_{exp}[c]/K	J_{exp}[d]/K
S-NPs	123	0.2495	+279.715	+66.89
D-NPs	73	0.2897	+254.913	+41.54

[a] The T_{conv} refers to the transition temperature of the $\chi_m T$ curve. [b] θ (K) represents the Weiss temperature. [c] Obtained from SQUID. [d] Obtained from VT-EPR.

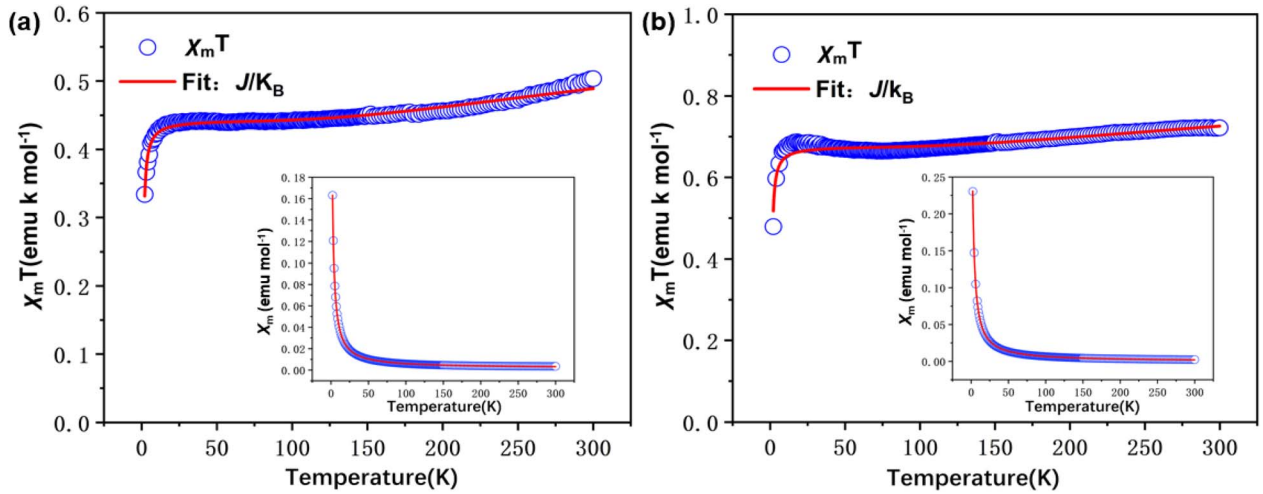

Fig. 9 SQUID magnetometry of solid samples: plots of $\chi_m T$ *vs.* T at $H = 10\,000.31543$ Oe in the warming mode (blue circle). Inset plots: χ_m *vs.* T in the warming mode and fitting (solid red line) curves of (a) **S-NPs**; (b) **D-NPs**. The drawing data is subtracted from the background.

be ferromagnetic. This was confirmed by subsequent SQUID analysis as well.

$$\mathrm{IT} = \frac{C}{3 + \exp\left(-\frac{2J}{K_B T}\right)} \quad (1)$$

SQUID. The SQUID characterization of the prepared self-assembled gold nanoparticle solid samples was carried out (Fig. 9). The aggregated magnetic behavior of the two prepared samples was determined at different temperatures to identify the ground state and triplet state of the biradicals involved in the self-assembly. The diamagnetic susceptibility of all samples was deducted using Pascal's table,[37] considering both the magnetic properties of radicals and **NPs**, which differs from conventional condensed matter.

In order to obtain the relevant parameters of the sample by fitting the test curve, we used the Hamiltonian $H = -2JS_1S_2$ (where $S_1 = S_2 = 1/2$). The processed data were corrected and calculated as χ_m *vs.* T and $\chi_m T$ *vs.* T, and fitted using the Bleaney–Bowers eqn (2).[38]

$$\chi_m T = (1 - F)\frac{2N_A g^2 {\mu_B}^2}{k_B}\frac{1}{3 + \exp\left(-\frac{2J}{k_B T}\right)}\frac{T}{T - \theta} + F\frac{N_A g^2 {\mu_B}^2}{k_B} \quad (2)$$

where, J represents the intramolecular exchange of diradicals; θ represents the generalized mean field of intermolecular exchange; N_A represents the Avogadro number, g represents the isotropic g-factor, k_B represents the Boltzmann constant, μ_B represents the Bohr magneton and F represents the paramagnetic impurity. J, θ and Lande'g factors are fitted parameters.

Measurements were performed over the temperature range of 2–300 K at a fixed field strength of 10000 Oe. According to the results fitted by eqn (2), both **S-NPs** and **D-NPs** exhibit strong ferromagnetism: $J_{\text{S-NPs}} = +279.715$ K and $J_{\text{D-NPs}} = +254.913$ K, the results with the J obtained from VT-EPR were shown in Table 4. The $\chi_m T - T$ curve of the **S-NPs** and **D-NPs** exhibited temperature dependence during the warming process. At 300 K, the $\chi_m T$ of **S-NPs** reaches approximately 0.490 cm^3 K mol^{-1}, which exceeds the theoretical value of 0.375 cm^3 K mol^{-1} for single radicals. This can be attributed to the strong ferromagnetic coupling interaction. When the temperature is cooled down from 300 K to 58 K, the value of $\chi_m T$ decreases slowly and uniformly. This can be explained to the slightly intermolecular antiferromagnetic coupling. As the temperature decreases from 58 K to 23 K, the $\chi_m T$ value exhibits a slight increase, illustrating the ferromagnetism in **S-NPs**. At 300 K, the $\chi_m T$ of **D-NPs** reaches approximately 0.770 cm^3 K mol^{-1}, which is basically consistent with the theoretical value of 0.750 cm^3 K mol^{-1} for the diradical. The $\chi_m T$ gradually decreased during cooling from 300 K to 73 K. This is mainly due to the slightly intermolecular antiferromagnetic coupling caused by the spatial motion of the radical-connected soft chains in the high-temperature region. Upon further cooling from 73 K to 25 K, the $\chi_m T$ of **D-NPs** shows a relatively obvious increase. This illustrates the ferromagnetism in **D-NPs**.[39,40]

The first striking feature to be observed in the M-H magnetization reversal loops is the presence of hysteresis and a remnant magnetization, all indicative of ferromagnetic behavior (Fig. 10) at both room temperature 1.9 K and 300 K. The M value is higher than that of the previously reported alkyl mercaptan modified gold nanoparticles,[35] indicating the presence of better ferromagnetism. Among them, the M of **D-NPs** is higher than **S-NPs**, which is consistent with magnetic analysis from χmT *vs.* T and VT-EPR.

We compared the magnetic properties of **S-NPs** with **D-NPs**. The J value of **S-NPs** is slightly larger than **D-NPs**. The two **NN** groups which are meta-connected on the benzene have an intramolecular ferromagnetism of 23 K.[36] The intramolecular interactions are present in **D-NPs** while absent in **S-NPs**. Besides, intermolecular spin interactions through space are generally antiferromagnetic.[41] The radical packing density of **D-**

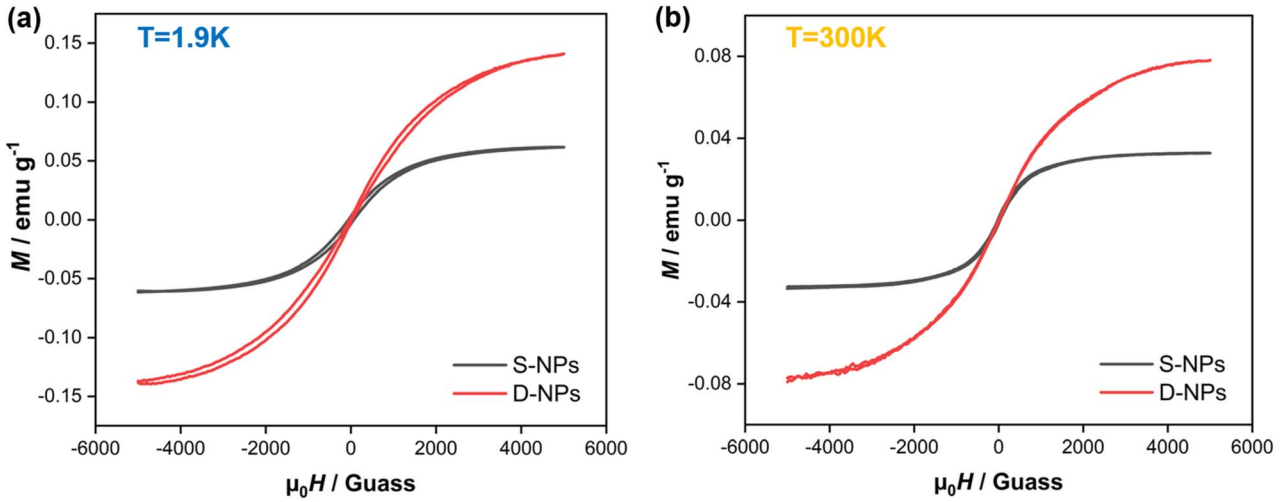

Fig. 10 Magnetization reversal loops measured at (a) 1.9 K and (b) 300 K.

NPs is 4.75 times higher than **S-NPs**, resulting in a stronger intermolecular antiferromagnetism through space directly. The combined effect of intramolecular interactions and spin interactions through space results in the J value of **S-NPs** being slightly larger than **D-NPs**. The occurrence of ferromagnetism at Au–S interfaces has been observed, and the ferromagnetism has been associated with Au 5d localized holes that are the result of charge transfer from the Au surface atoms to the S atoms of the organic ligands when forming the Au–S bonds.[35,42] There are A–S bond on Au surface in both **S-NPs** and **D-NPs**, and we refer to the resulting ferromagnetism as spin interactions through the gold surface. It can be deduced that the considerable ferromagnetism in **S-NPs** and **D-NPs** should be attributed to the spin interactions through Au surface primarily. This analysis also suggests that the strategy of achieving close-packing through Au–S self-assembly to obtain a material with strong magnetic coupling is a feasible approach.

Conclusions

Herein, a series of self-assembled organic spin hybrid samples were prepared based on the **AuNPs** by utilizing the binding of Au–S bonds and innovatively choosing **NN**-type double radicals. The accuracy of the structural synthesis of the samples was verified by UV, IR, MS, Raman spectrum and CV tests. The morphology and radical packing density of the samples were discussed by TEM and EDS. The magnetic properties of the samples were investigated and analyzed by use EPR and SQUID. The results of packing density analysis indicate that the self-assembled strategy employing two radicals achieved higher packing densities on the gold surface and that the **D-NPs** achieved higher packing densities on the **AuNPs** surface than those previously reported for **NN** type radicals. Magnetic analysis showed that **S-NPs** and **D-NPs** exhibited a higher ferromagnetism than previously reported alkyl mercaptan modified gold nanoparticles and most of **NN** type organic radicals, which is the superposition of the ferromagnetism due to the Au 5d localized holes on the gold surface and the spin magnetism of **NN**. Besides, it shows that the use of the radical self-assembly strategy on the gold surface is a promising approach for synthesizing macroscopic ferromagnets in the aggregated state. In addition, **AuNPs** with magnetic properties have a wide range of applications in the biomaterials, such as drug targeting, magnetic imaging. This study provides a valuable strategy for the preparation of organic magnetic hybrid magnets with tightly ordered organic spin structures.

Data availability

The data supporting this article have been included as part of the ESI.†

Author contributions

Zhipeng Xu: conceptualization, investigation, writing – original draft. Dongdong Wei: investigation, validation. Yongliang Qin: formal analysis. Jie Jin: supervision. Long Zheng: resources. Jie Xu: software. Hui Liu: methodology. Ranran Chen: resources. Di Wang: funding acquisition, writing – review & editing.

Conflicts of interest

There are no conflicts to declare.

Acknowledgements

This work was supported by the following funds: National Natural Science Foundation of China (No. 52003004), Anhui Provincial Outstanding Youth Scientific Research Project (No. 2023AH030036), China Railway Scientific Research Project (HYB20200183). Natural Science Foundation of Anhui Province (2108085QE216), Natural Science Foundation of the Anhui Higher Education Institutions (2022AH050243).

Notes and references

1 A. E. Thorarinsdottir and T. D. Harris, *Chem. Rev.*, 2020, **120**, 8716–8789.
2 R. A. Layfield, *Organometallics*, 2014, **33**, 1084–1099.
3 I.-J. Baek and W.-J. Cho, *Solid-State Electron.*, 2018, **140**, 129–133.
4 W. Canon-Mancisidor, M. Zapata-Lizama, P. Hermosilla-Ibanez, C. Cruz, D. Venegas-Yazigi and G. Minguez Espallargas, *Chem. Commun.*, 2019, **55**, 14992–14995.
5 K. Taniguchi, M. Nishio, N. Abe, P. J. Huang, S. Kimura, T. H. Arima and H. Miyasaka, *Angew. Chem., Int. Ed. Engl.*, 2021, **60**, 14350–14354.
6 F. Liu, X. Hou, B. Hu and R. Li, *Molecules*, 2021, **26**, 6130.
7 K. Kolanji, P. Ravat, A. S. Bogomyakov, V. I. Ovcharenko, D. Schollmeyer and M. Baumgarten, *J. Org. Chem.*, 2017, **82**, 7764–7773.
8 M. Mas-Torrent, N. Crivillers, C. Rovira and J. Veciana, *Chem. Rev.*, 2012, **112**, 2506–2527.
9 A. C. Petre Ionita, B. C. Gilbert and V. Chechik, *J. Am. Chem. Soc.*, 2002, **124**, 9048–9049.
10 E. V. Tretyakov, P. A. Fedyushin, E. V. Panteleeva, D. V. Stass, I. Y. Bagryanskaya, I. V. Beregovaya and A. S. Bogomyakov, *J. Org. Chem.*, 2017, **82**, 4179–4185.
11 P. Ravat, Y. Borozdina, Y. Ito, V. Enkelmann and M. Baumgarten, *Cryst. Growth Des.*, 2014, **14**, 5840–5846.
12 R. Rausch, A. M. Krause, I. Krummenacher, H. Braunschweig and F. Wurthner, *J. Org. Chem.*, 2021, **86**, 2447–2457.
13 V. Lloveras, P. Elias-Rodriguez, L. Bursi, E. Shirdel, A. R. Go Experimental assistanceni, A. Calzolari and J. Vidal-Gancedo, *Nano Lett.*, 2022, **22**, 768–774.
14 S. Laurent, D. Forge, M. Port, A. Roch, C. Robic, L. Vander Elst and R. N. Muller, *Chem. Rev.*, 2008, **108**, 2064–2110.
15 D. Ling, N. Lee and T. Hyeon, *Acc. Chem. Res.*, 2015, **48**, 1276–1285.
16 T. Furui, S. Suzuki, M. Kozaki, D. Shiomi, K. Sato, T. Takui, K. Okada, E. V. Tretyakov, S. E. Tolstikov, G. V. Romanenko and V. I. Ovcharenko, *Inorg. Chem.*, 2014, **53**, 802–809.
17 R. Tanimoto, T. Wada, K. Okada, D. Shiomi, K. Sato, T. Takui, S. Suzuki, T. Naota and M. Kozaki, *Inorg. Chem.*, 2022, **61**, 3018–3023.
18 Z. Yue, J. Liu, M. Baumgarten and D. Wang, *J. Phys. Chem. A*, 2023, **127**, 1565–1575.
19 D. Wang, Y. Ma, B. Wolf, A. I. Kokorin and M. Baumgarten, *J. Phys. Chem. A*, 2018, **122**, 574–581.
20 B. Mladenova-Kattnig, G. Grampp and A. I. Kokorin, *Appl. Magn. Reson.*, 2015, **46**, 1359–1366.
21 Y. Gao, J. Hu and Y. Ju, *Acta Chim. Sin.*, 2016, **74**, 312–329.
22 V. Loveras, E. Badetti, J. Veciana and J. Vidal-Gancedo, *Nanoscale*, 2016, **8**, 5049–5058.
23 Y. Wang, N. S. Hush and J. R. Reimers, *J. Am. Chem. Soc.*, 2007, **129**, 14532–14533.
24 M. S. Inkpen, Z. F. Liu, H. Li, L. M. Campos, J. B. Neaton and L. Venkataraman, *Nat. Chem.*, 2019, **11**, 351–358.
25 Y. Ohya, N. Miyoshi, M. Hashizume, T. Tamaki, T. Uehara, S. Shingubara and A. Kuzuya, *Small*, 2012, **8**, 2335–2340.
26 J. Hu, R. Jiang, H. Zhang, Y. Guo, J. Wang and J. Wang, *Nanoscale*, 2018, **10**, 18473–18481.
27 S. Rautiainen, J. Chen, M. Vehkamäki and T. Repo, *Top. Catal.*, 2016, **59**, 1138–1142.
28 P. D. Ortiz, J. Castillo-Rodriguez, X. Zarate, R. Martin-Trasanco, M. Benito, I. Mata, E. Molins and E. Schott, *Langmuir*, 2018, **34**, 9402–9409.
29 D. J. Lavrich, S. M. Wetterer, S. L. Bernasek and G. Scoles, *J. Phys. Chem. B*, 1998, **102**, 3456–3465.
30 C. K. A. Nyamekye, S. C. Weibel and E. A. Smith, *J. Raman Spectrosc.*, 2021, **52**, 1246–1255.
31 X. Feng, J. Yang, X. Duan, Y. Cao, B. Chen, W. Chen, D. Lin, G. Qian, D. Chen, C. Yang and X. Zhou, *ACS Catal.*, 2018, **8**, 7799–7808.
32 C. Qi, Y. Cheng, Z. Yang, T. Ishida, H. Su, J. Zhang, X. Sun, L. Sun, L. Zhao and T. Murayama, *J. Catal.*, 2024, **436**, 11560.
33 U. Eichhoff and P. Höfer, *Appl. Magn. Reson.*, 2020, **51**, 1723–1737.
34 S. Hase, D. Shiomi, K. Sato and T. Takui, *J. Mater. Chem.*, 2001, **11**, 756–760.
35 P. Dong, E. A. Fisher, M.-V. Meli and S. Trudel, *Nanoscale*, 2020, **12**, 19797–19803.
36 M. E. Ali and S. N. Datta, *J. Phys. Chem. A*, 2006, **110**, 2776–2784.
37 G. A. Bain and J. F. Berry, *J. Chem. Educ.*, 2008, **85**, 532–536.
38 C. Shi, L. Gao, M. Baumgarten, D. Wei, Z. Xu, W. Wang and D. Wang, *Magnetochemistry*, 2023, **9**, 178.
39 K. Tanaka, K. Furuichi, M. Kozaki, S. Suzuki, D. Shiomi, K. Sato, T. Takui and K. Okada, *Polyhedron*, 2007, **26**, 2021–2026.
40 L. Catala, J. Le Moigne, N. Kyritsakas, P. Rey, J. J. Novoa and P. Turek, *Chem. - Eur. J.*, 2001, **7**, 2466–2480.
41 T. Mitsumori, K. Inoue, N. Koga and H. Iwamura, *J. Am. Chem. Soc.*, 1995, **117**, 2467–2478.
42 M. Suda, N. Kameyama, M. Suzuki, N. Kawamura and Y. Einaga, *Angew. Chem.*, 2008, **120**, 166–169.